

Physics first, using ANSYS to define the design: Real-life examples from the automotive supplier company Mannesmann VDO

Zlatko Penzar

Mannesmann VDO AG, Fuel Systems
Schwalbach, Germany
penzar01@de1.vdogrp.de

Summary:

In many non-standard engineering development applications it strongly pays off to invest an effort into understanding the physics of the problem prior to undertaking complex numerical simulations. The better the knowledge of the leading physical effects in a complex system, the simpler and more cost-efficient the analytical model can be. Moreover, the understanding of the most important physical driving effects often enables one to build a simplified, closed-form mathematical effective model. Such models usually give insight into the interplay of various parameters governing the physical behavior of the complex system. In this way, a fast pre-optimization of the desired features is often possible. Subsequently, the rich arsenal of ANSYS multiphysics capabilities can be used to refine the judgements and obtain the desired quantitative solutions.

We shall present three examples from our company's engineering development activity:

- 1) A new magnetic-mechanical automotive position sensor, MAPPS, where simple closed-form expressions enabled the insight into the relations between the following counteracting goals: Magnetically induced contact forces as high as possible, favoring soft mechanical spring characteristics and on the other hand the requirement of the lowest allowed eigenfrequency value, favoring the stiffness increase.
- 2) A simple procedure of calculating the crash or drop-test performance of the closed containers, partially filled with fluid, being applicable to automobile fuel tanks.
- 3) Torque sensor for electric power-steering applications, where the studies of the related FEA results, a posteriori, lead to closed-form mathematical models, revealing how the same device can be alternatively used as a bending-moment or a shear force sensor. In this way, more than the originally desired goal has been achieved!

Keywords:

ANSYS/multiphysics, physical simplification, effective models, closed-form-math, automotive sensors, ANSYS/LS-DYNA, impact performance of fluid-filled containers.

In the following chapters we shall demonstrate three completely different ANSYS applications. The only unifying property of these applications is that a lot of effort was first invested in attempting to understand the non-trivial physics of these problems, resulting in relatively simplified closed-form math effective models, or simple physical models. This considerably simplified subsequent ANSYS analyses, which would otherwise have been tremendously difficult.

1 MAPPS

In this chapter we present our pre-optimization of the contact spring in our new **MA**gnetic **P**assive **P**osition **S**ensor (MAPPS) (Fig. 1).

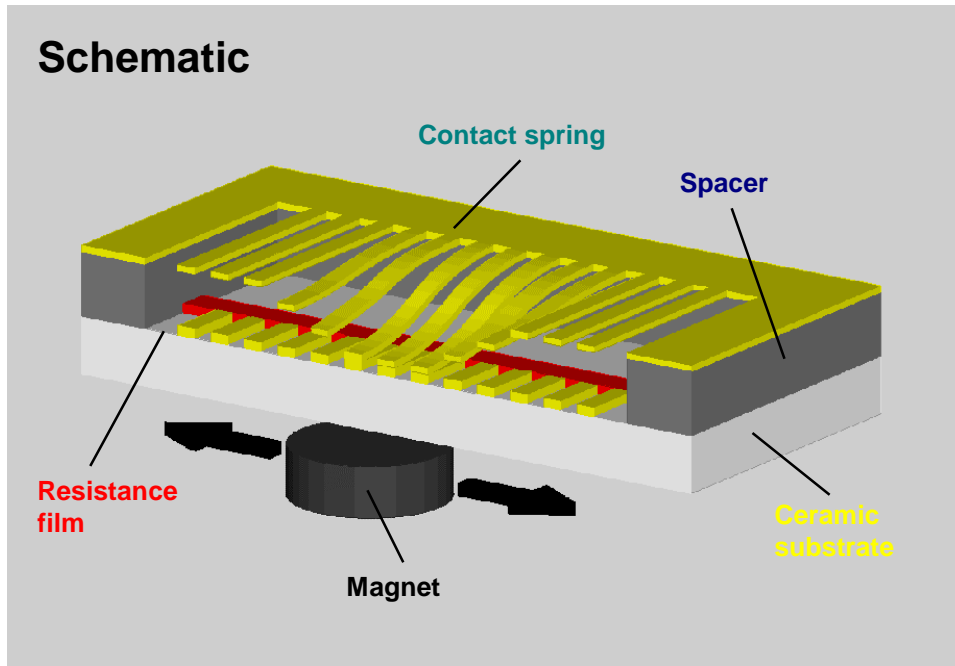


Fig. 1
Schematic figure of MAPPS (Magnetic Passive Position Sensor)

The device consists in principle of a thin sheet, magnetically permeable metal spring, hermetically encapsulated in a housing. Outside the housing, a permanent, movable magnet is positioned. The magnet attracts a few closest spring fingers, which then move and contact the resistor plate within the housing. In this way, the resistance of the device changes with the position of the magnet. The device is an ideal position sensor, being able to operate in the arbitrary aggressive media, which could otherwise endanger the contact quality in an open-contact system. Its first industrial application will be in the fuel gage (the magnet is mounted on a lever arm, with the float at the other end, thus moving with the fuel level in the tank). Other automotive position sensor applications are being envisaged as well.

1.1 Goals in optimizing the spring:

- 1) Maximize the contact force: Contact force = magnetic attractive force **minus** the mechanical spring return force at contact position.
- 2) At the same time: The lowest eigenfrequency must lie above 1000 Hz (cycles/sec).

It would be very trivial to enhance the contributions concerning the goal 1), i.e. enhance the contact force in itself. For example, by designing the spring paddles as soft as possible (e.g. by using very long spring finger arms in Fig. 2) we could tune the spring return force virtually down to zero. However, in this case the condition 2) would not be fulfilled. The contact springs could exhibit large oscillation amplitudes under normal vibrations in the car, thus contacting and yielding a spurious signal.

Furthermore, the magnetic attractive force can be enhanced by enlarging the pad area at the free ends of the contacting fingers, and/or by increasing the thickness of the metal sheet. However, the first of these measures increases the vibrating mass and therefore lowers the eigenfrequency and the second one enhances the spring return force and therefore lowers the contact force!

Finally, the knowledge about the allowed metal sheet thickness range, its material mechanical properties as well as its magnetic properties such as saturation magnetization and coercive field boundaries crucially defines the available sheet manufacturing technologies, **and therefore also the price.**

So, the above problem is a genuine coupled-field optimization task, which can, of course, be solved by straightforwardly applying the arsenal of ANSYS multiphysics and optimization tools.

However, there exists a shortcut way, separating-out the leading physical effects in question and getting insight into their mutual interdependence.

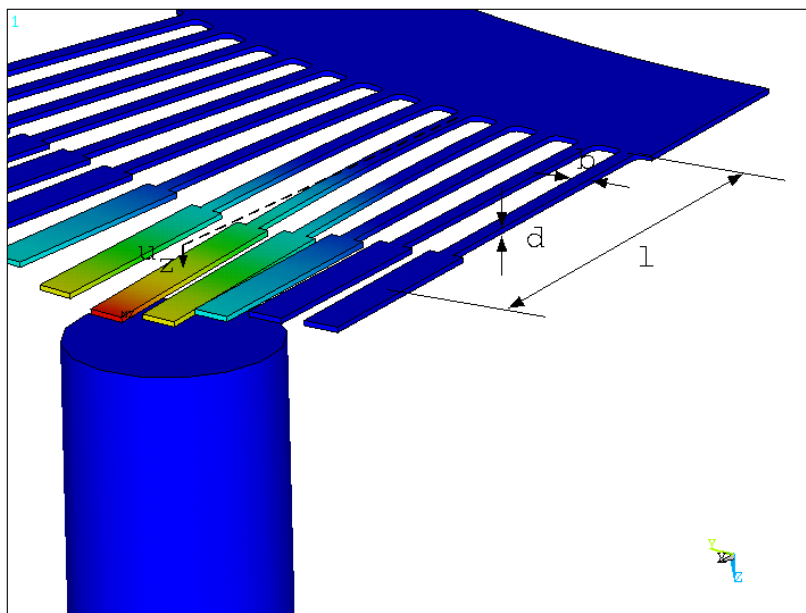


Fig. 2
FE-model of the most important components in the mechanical-magnetic circuit of MAPPS.

1.2 A simplified magnetic-mechanical model

To do this, we shall build up an effective, simplified model, based on the following approximations (for clarity see Fig. 2):

- a) The entire magnetic attractive force originates from the broad pads at the free end of the contact fingers.
- b) The entire spring characteristics are governed by the long finger cantilever beams.
- c) The total vibrating mass is concentrated in the pads at the free ends of the contacting paddles. (The thin spring fingers are massless).

Although the above assumptions are only a simplification (of course, some magnetic force comes in from the long finger regions, and a small inertia contribution from the mass in the fingers influences the vibration), this approximation contains the leading physical contributions. Especially the comparatively long lever arms of the contacting fingers dictate that the decisive magnetic attractive force and vibration mass contributions originate from the pad regions (Fig. 2). On the other hand, the contribution of the pad region elasticity is negligible in comparison to the elasticity of the long cantilever beams, concerning the displacements at the tip of the contact paddles.

1.2.1 Magnetic force

The magnetic force \vec{F}_M on an object with magnetization density \vec{M} in the **external** magnetic field \vec{B}_e is equal to [1]

$$(1) \quad \vec{F}_M = - \int (\vec{\nabla} \cdot \vec{M}) \vec{B}_e d^3x .$$

For a thin plate at magnetic saturation, the absolute value of the magnetization density \vec{M} has nearly a constant value

$$(2) \quad M = \frac{1}{4\pi} B_S ,$$

within the material [2], where B_S is the saturation magnetization field of the material. If the external field \vec{B}_e is oriented normal to the plate, the only significant contribution of the divergence of the magnetization density in the formula (1) originates from the surface regions, where the magnetization density abruptly drops from the value in eq. (2) down to zero. So, the integral (1) can be rewritten as

$$(3) \quad F_M = \frac{1}{4\pi} \int B_S (B_{e,N}^{\text{top}} - B_{e,N}^{\text{bottom}}) d^2x$$

where $B_{e,N}^{\text{top}}$ and $B_{e,N}^{\text{bottom}}$ are the normal components of the **external** magnetic field at the top and the bottom plate surface, respectively. The integral in eq. (3) runs over the 2D-surface coordinates of the plate.

The difference between the external magnetic field values on the top and the bottom surface of the plate, appearing in eq. (3) can in the first approximation be written as

$$(4) \quad B_{e,N}^{\text{top}} - B_{e,N}^{\text{bottom}} = d \cdot \nabla_N B_{e,N}$$

where ∇_N is the gradient in the normal direction to the plate, evaluated in the middle between the plate surfaces and d is the plate thickness.

Using eq. (4), the expression (3) can be re-written as

$$(5) \quad F_M = \frac{1}{4\pi} \int B_S d (\nabla_N B_{e,N}) d^2x = \frac{1}{4\pi} B_S \cdot d \cdot A \cdot \overline{(\nabla_N B_{e,N})} ,$$

where A is the total surface area of the permeable magnetic plate and $\overline{(\nabla_N B_{e,N})}$ the mean value of the gradient in the normal direction, of the normal component of the **external** magnetic field, averaged over the surface of the plate.

The formula (5) illustrates among other things the known fact, that the magnetic force on a magnetic plate does not depend directly on the **strength** of the external magnetic field B_e , but on its **gradient**.

There is no magnetic attraction in a homogeneous external field!

1.2.2 Vibration frequency

For our idealized model the lowest vibration eigenfrequency, f , of a single paddle is that of a spring-mass system with a spring constant k and a mass m :

$$(6) \quad f = \frac{1}{2\pi} \sqrt{\frac{k}{m}};$$

with

$$(7) \quad k = E \frac{b \cdot d^3}{4l^3} \text{ (a cantilever beam bending stiffness), and}$$

$$(8) \quad m = \rho \cdot d \cdot A.$$

In the expressions above, b is the spring finger width, d , the metal sheet thickness and l the length of the spring paddle from the clamped end up to the center of mass of the magnetic pad (Fig. 2). E is the Young's elasticity modulus of the material. A is the area of the contact pad and ρ the density of the material.

From our experience concerning the vibration spectra in vehicles, the eigenfrequency f should not lie under the value of $f_0 = 1000 \text{ Hz}$.

The lowest allowed frequency is the most favorable one, concerning the requirement of the maximum contact force requirement. For this, it follows from (6):

$$(9) \quad k = (2\pi)^2 f_0^2 \rho A d$$

1.2.3 Contact force

The contact force F_K is the difference between the magnetic attractive force F_M and the spring return force, $k \cdot u_z$, where u_z is the displacement of the contact pad from the zero-magnetic-field-equilibrium up to the contact position (Fig. 2)¹:

$$(10) \quad F_K = F_M - k u_z$$

Using expressions (5) and (9) in the equation (10) one obtains:

$$(11) \quad F_K = d \cdot A \cdot \left[\frac{1}{4\pi} B_S \cdot (\nabla_N B_{e,N}) - 2\pi^2 f_0^2 \rho u_z \right]$$

Employing (7) in (9) one obtains an additional dependence:

$$(12) \quad E \frac{b \cdot d^2}{4\rho A l^3} = (2\pi)^2 f_0^2$$

Equations (11) and (12) contain all the desired relations: In order to attain a desired contact force F_K there is an optimal relation between the geometric parameters of the contact pads d and A ,

¹ For simplicity, we have written down the contact force expressions, assuming that the mechanical contact originates at the position of the pad center of mass. If the mechanical contact originates predominantly at the tip of the contacting fingers, lever-arm corrections for force and displacement have to be included. However, beside a few slightly lengthier expressions, this does not enhance the complexity whatsoever, entirely retaining the basic strategy and the quality of the achievable results.

contacting displacement u_z , the gradient of the external magnetic field B_e and of the saturation magnetization field value B_S . The further relations between the geometry parameters, Young's elasticity modulus and the density in the equation (12) guarantee that the system has the lowest allowed eigenfrequency f_0 .

The expressions (11) and (12) are by no means exact. However, they describe fairly accurately the relations between the numerous geometric, field and material parameters and thus enable first of all, fast studies on the feasibility of the design, and furthermore, the search restrictions concerning the possibilities of material choice (and price!) and an extremely fast pre-optimization of the geometry!

Afterwards, when the decision on the materials choice and a nearly-optimal shape had been met, several detailed coupled-field magnetic-mechanical ANSYS calculations have been performed, refining the judgements above. In this way, the results for the final design fixing have been generated.

In practical tests this FEA-optimized design turned out to behave exactly as desired, having also very high safety margins concerning the desired properties, and thus generally a high robustness. The SOP is due soon.

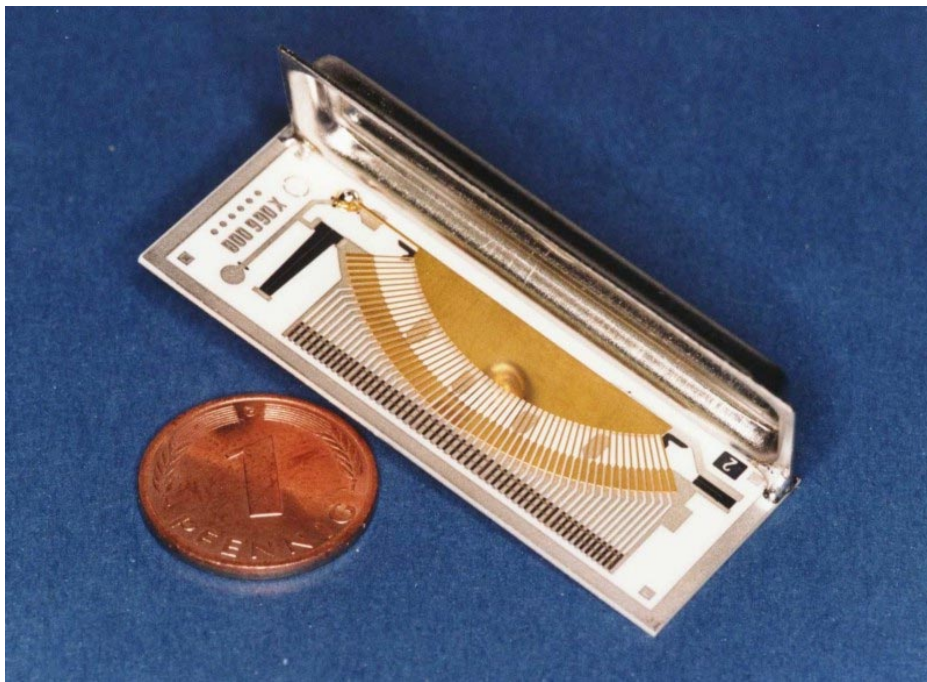


Fig. 3
MAPPS sample, with its mechanical-magnetic spring geometry, resulting from the above math and ANSYS optimization.

2 Impact performance of closed tanks, filled with fluid

In this second example we shall present a simple method, allowing us to investigate the impact performance of containers, partly filled with fluid. We apply this procedure in studying the corresponding performance of fuel tanks under e.g. drop or sledge impact tests.

It is very difficult and resource-consuming to couple genuine CFD and mechanical FE codes to attain a fully self-consistent coupled dynamical simulation of a fluid with the free surface, contained in a container under arbitrary time-dependent loads.

If only a moderate sloshing movement of fuel (away from the turbulent regime) is of interest, the Euler-Lagrange formulation can be used, allowing the transport of fluid matter and the movement of the free surface, as has been done e.g. in LS-DYNA. A strong progress in this direction has been (so far only 2D) achieved also within ANSYS-FLOTRAN.

The primary interest of our specific applications is to study whether a closed container with fluid would survive the moment of highest material loading upon impact.

In these cases, the container with fluid moves at the beginning with a uniform velocity. Upon impact, the container wall is stopped and is being deformed by the impact barrier. The fluid itself would, however, like to move on, governed by its inertia. If the impact barrier is positioned in the direction of the container movement, it prohibits the further movement of the fluid in this initial direction. However, the impact barrier acts as a source of strong momentum exchange, leading to a sideward motion of the fluid. In the first instance, the fluid attempts to keep its kinetic energy by moving sideward and over the free surface in the original direction of motion, because the fluid layers can easily glide with respect to each other (Figs. 4, 5). When the fluid finally has no other free room within the container for escaping and changing its position and/or direction of movement in such a way, it presses on the container walls. As the fluid is almost incompressible, it develops a strong pressure pulse on the container walls, while being stopped.

This pressure pulse is the most important source of the fluid contribution to the additional container wall material loading upon impact at its most dangerous stage.

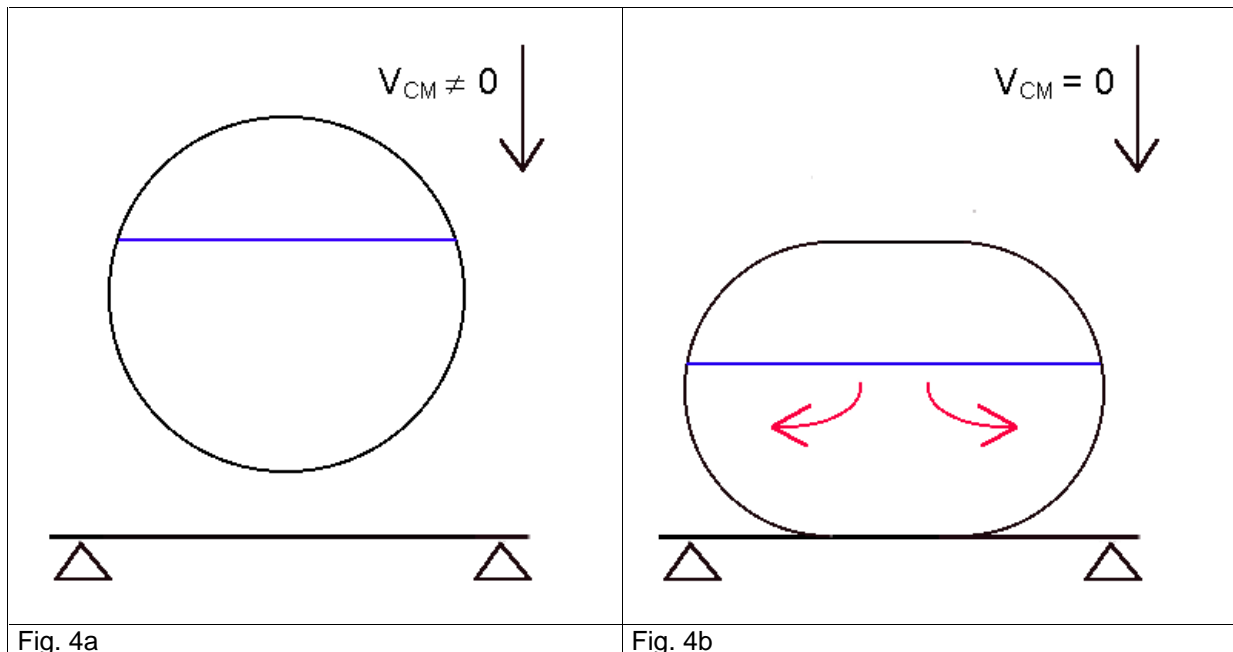


Fig. 4

Schematic movement of a deformable container filled with fluid upon a drop-test. Fig. 4a: fluid and container move with a uniform velocity, equal to their center of mass velocity $V_{CM} \neq 0$, towards the hard wall. Fig. 4b: The moment at which the center of mass velocity of the container + fuel comes to halt, $V_{CM} = 0$. The deformed container shape as well as the dominant movement of the fuel layers (red arrows) are schematically shown.

The above scenario can be relatively easily implemented in the FE codes, without introducing a too sophisticated fluid-solid coupling.

The most important physical properties of the fluid during the buildup of this first pressure pulse are:

- a) fluid layers can glide very easily with respect to one another
- b) fluid is almost incompressible.

We can get these physical properties to work in a following way:

- Model the fluid by 3D solid elements and tune the shear modulus to virtually zero (as low as the algorithms work in a stable way).
- Keep the compressibility modulus the same as for the real fluid.
- Position the contact elements between the container shell and the fluid, in order to prevent fluid penetration through the shell.

- If necessary, in addition to the virtually zero value of the shear modulus, introduce fluid material yielding (elastic-plastic).

The above procedure can be done within ANSYS, by e.g. taking the elastomere elements for fluid, since they are designed to work for almost incompressible media.

As we are predominantly interested in strong impact phenomena, we applied the above recipe within ANSYS/LS-DYNA.

An illustration of the procedure is shown below:

A sphere, partly filled with fluid (gasoline) uniformly moves and hits the hard wall. The sloshing of the fuel, the pressure pulse and the coupling between the movement of the fuel and the container are properly reproduced.

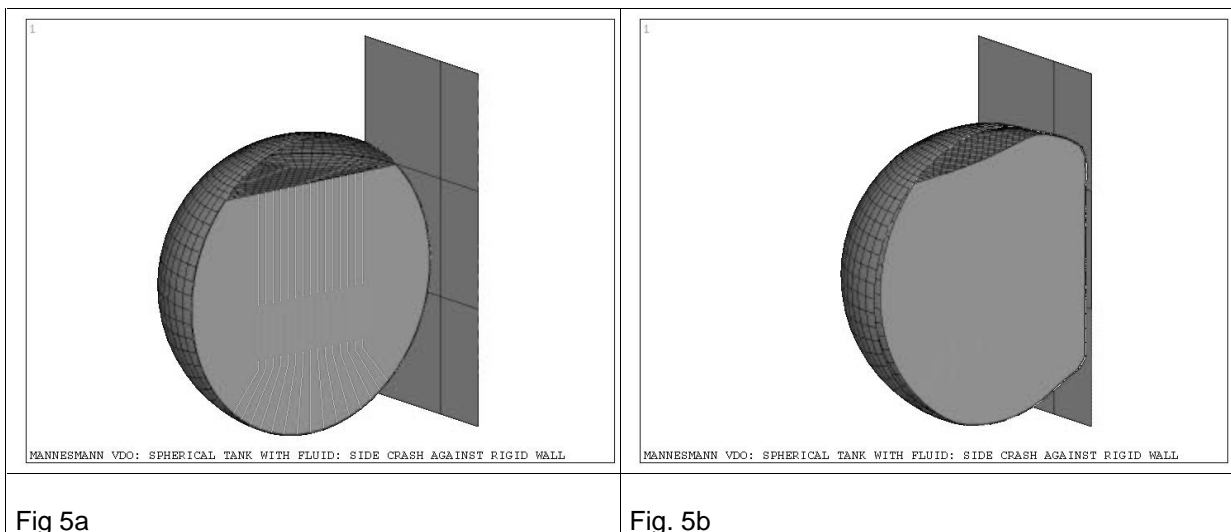


Fig.5

Test calculation: A container, partly filled with fluid hits a hard wall. In the calculation, the container is closed. Only one half of it, cut through its middle, is shown. 5a: Before impact. 5b. upon impact.

Of course, the movement of the fuel after this first impact shock is more complicated than can be obtained from the above described procedure. Often the complicated sloshing and even creation of foam sets in. These secondary phenomena are of course beyond the possibility of the present procedure. However, the main features at the onset of sloshing and the first pressure buildup are reproduced fairly well. This is, however, the most critical moment for the container. If it survives this first pressure buildup, it will survive the whole impact. And this is the scope of our investigations.

Our practical tests have shown, that the present procedure calculates pressure pulses, which are about 25% higher than in reality. This is sufficient for the most of our estimations concerning the impact performance of containers. Moreover, this type of estimations turned out to predict pressures on the safe side of pressure variations.

This procedure runs extremely fast, as fast as any mechanical, dynamical 3D calculation with contacts. If used properly, in studying a class of scenarios where applicable, it can be a very fast, powerful tool in investigating the impact performance of containers, filled with fluid. In addition, some sloshing phenomena can be studied as well.

3 Torque sensor

In this third example we report on a unusual consequence of a numerical optimization: After completing a number of numerical studies on a new torque sensor for power-steering applications we noticed that some features of these results can be rationalized through simple closed-form mathematical expressions. These expressions straightforwardly revealed that the sensor can be also used for other sensing applications: e.g. as a bending and shear force sensor, far more then was originally desired.

The sensor element consists in principle of a steel slab, which is being deformed under torsion.

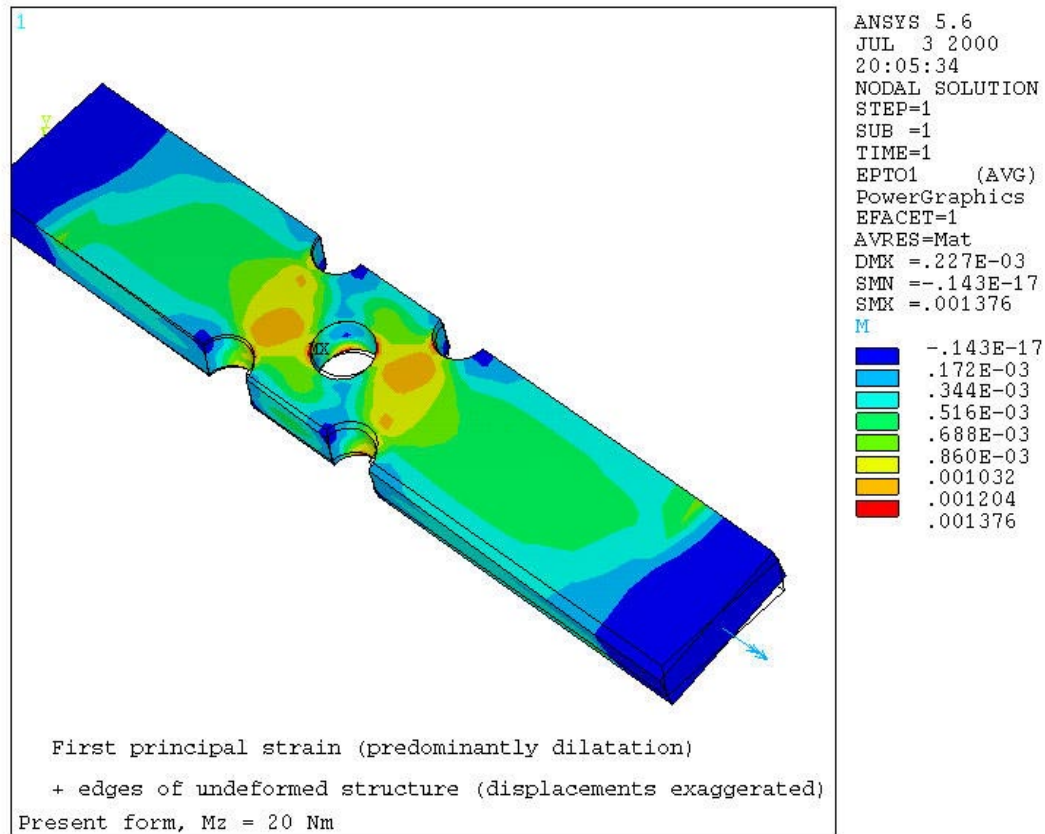


Fig.6.

Sensor body under torsion load. The top left end on the figure is firmly clamped. A torsion moment of 20 Nm around the main axis of the sensor (z-axis in Fig. 10) is applied at another end of the slab (bottom right end in Fig. 6, same as the “free end” in Fig. 10).

On the flat surface of the slab there are 4 ceramic resistors, bonded to the metal surface. The resistors are positioned point-symmetrically with respect to the central hole in the slab (Fig.7).

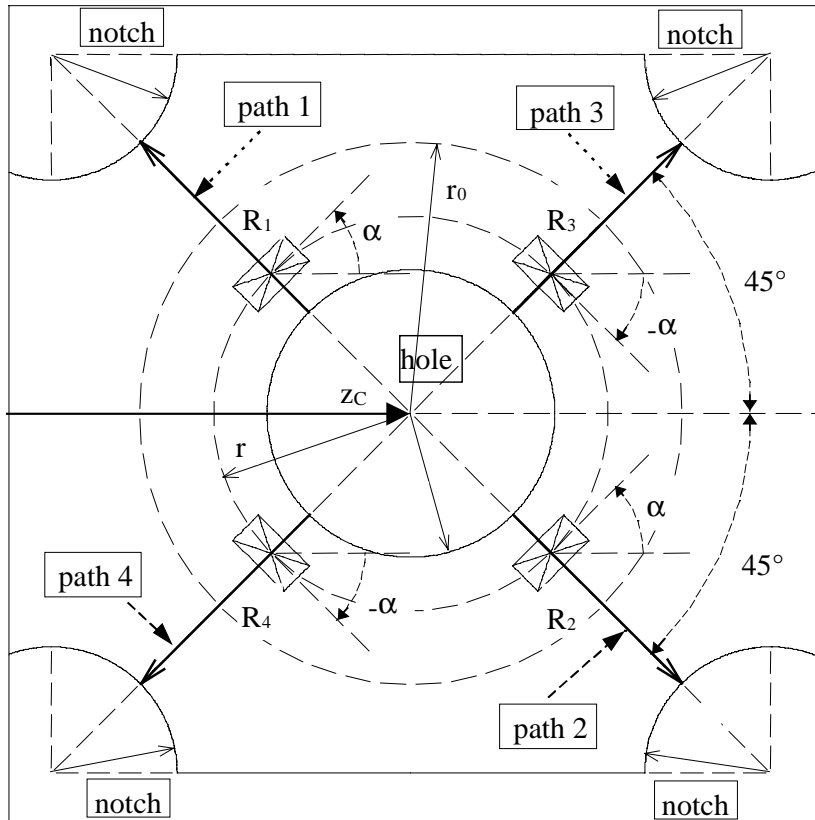


Fig.7

Positions of the four resistors, R_i ($i = 1,2,3,4$) on the slab surface z_C is the z -coordinate of the middle of the central hole (coordinate system shown in Fig. 10).

Upon a deformation of the sensor, the surface strains influence the relative resistance change on each of the resistors:

$$(13) \quad \frac{\Delta R_i}{R_i} = K_L \varepsilon_{L,i} + K_T \varepsilon_{T,i}, \quad (i = 1,2,3,4)$$

where $\varepsilon_{L,i}$ and $\varepsilon_{T,i}$ are the surface strains in the direction of the longitudinal axis (axis of the current) and normal to it, respectively, in the middle of the resistor i . K_L and K_T are the proportionality constants, which can be measured separately. So, the resistors sense a superposition of the surface strain along their axis and the one normal to it.

The simulation of the signal field given in expression (13) is shown in Fig.8. This signal field cannot be directly evaluated by default ANSYS options, but the vast postprocessing possibilities, using APDL enabled us to evaluate the linear combination of the fields in eq. (13) and impose it as a separate, artificial field to the FE-nodes of the structure (using DNSOL command). Afterwards, one can apply to it the entire arsenal of ANSYS postprocessing capabilities.

Not only that the overall strain level is higher in the channels between the central hole and the external “notches”, but also the strain field is such as to amplify a linear combination of particular strains leading to signal (13). The shape of the sensor has been strongly improved through FEA, in order to maximize this signal.

Through this FEA work, the torsion signal has been enhanced by more than a factor of 5 with respect to the starting design concept.

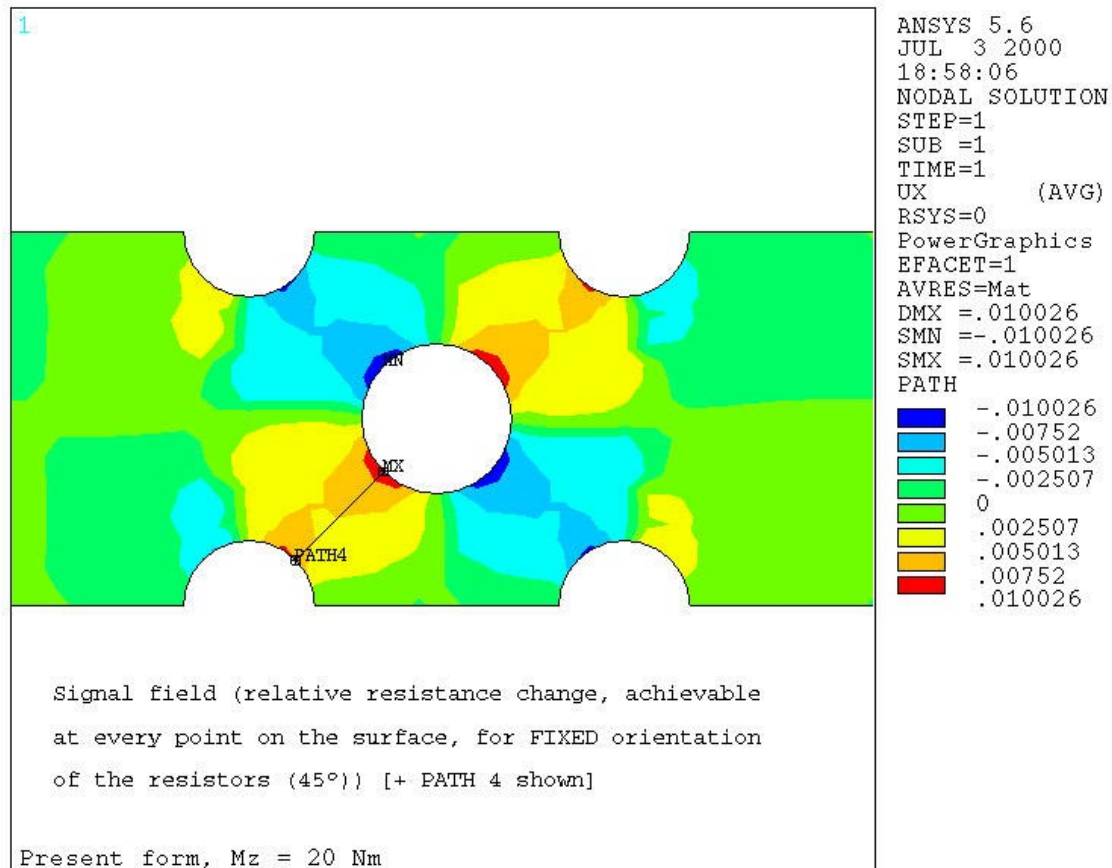


Fig. 8

The four resistors in Fig.7 are connected as a Wheatstone bridge (Fig. 9).

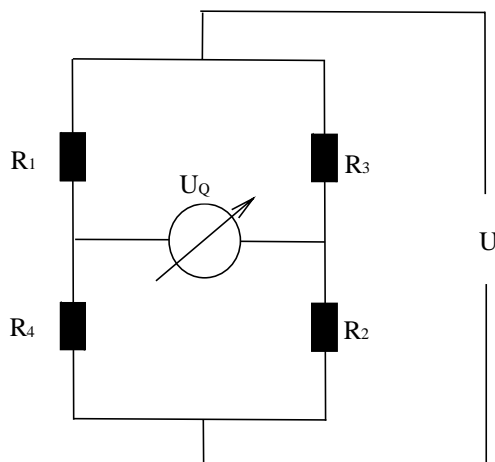


Fig. 9
Original resistor coupling scheme for a torsion sensor.

The bridge signal voltage according to the scheme in Fig. 9 is:

$$(14) \quad U_Q = U \cdot \frac{1}{4R} (\Delta R_1 + \Delta R_2 - \Delta R_3 - \Delta R_4)$$

This is the raw output of the sensor cell.

As shown in Fig.8, it is very convenient to position the four resistors along the four signal amplification channels, concerning the main effect, torsion deformation.

3.1 Undesired loads

However, when an undesired load, for example a bending moment or a shear force, normal to the main sensor axis (z-axis in Fig. 10) is applied, the sensor could nevertheless yield some signal, which is of course undesirable, since it could blur the main sensing effect: The sensor would signal torsion torque there where no such torque exists.

For this reason, we loaded the slab with bending moments and shear forces and studied the dependence of the relative resistance change of single resistors on the paths in Fig.7, as a function of their distance from the edge of the inner hole.

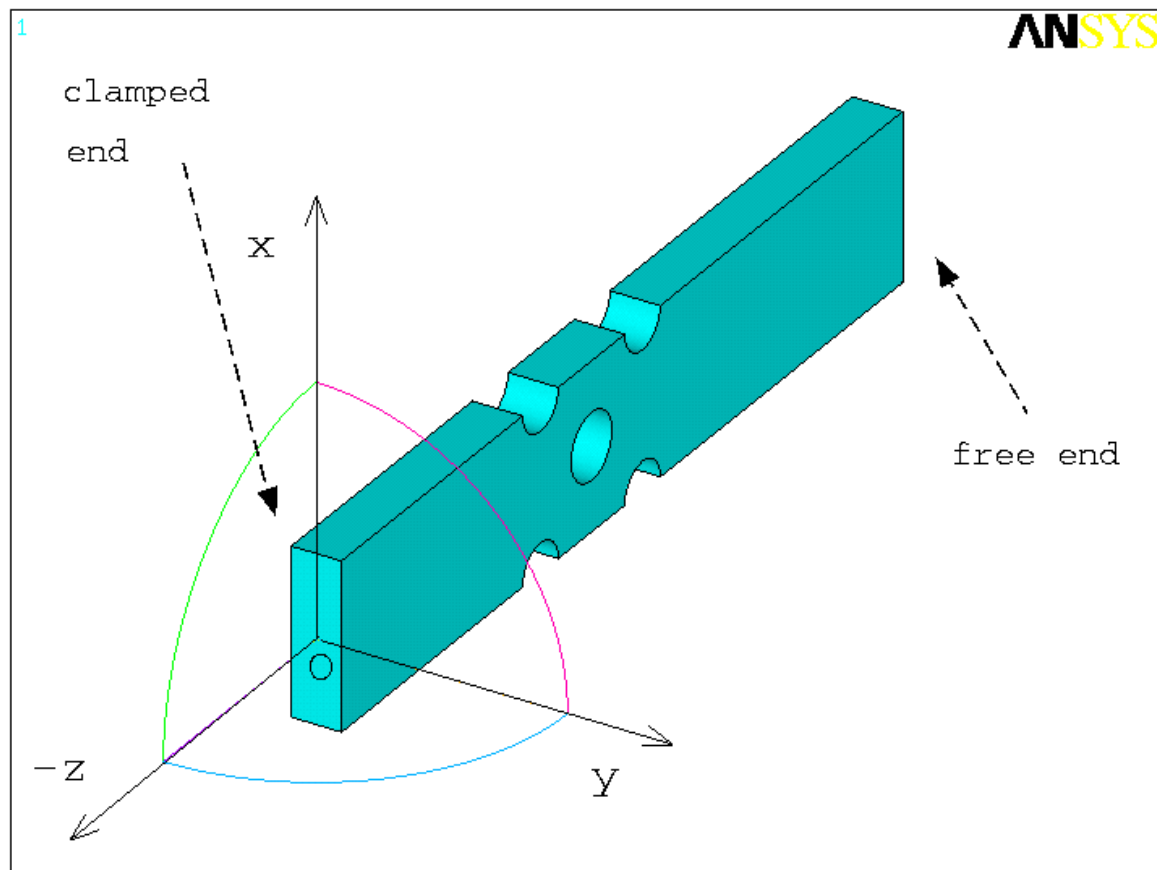


Fig. 10
Position of the sensor in the global coordinate system. In addition to the main investigated effect, the torsion moment loading about the z-axis at the free end (as in Fig.6), also the bending moment as well as the shear force loads, applied at the free end, in directions normal to the z-axis have been studied.

3.2 General bending load about the stiff axis

This is a case of a combined loading: A torque about the y-axis (M_y) and the shear force load in the x-direction, (F_x). Both loads are applied at the free end of the sensor (Fig. 10). Typical results for the resistors 1 and 3 behave like this

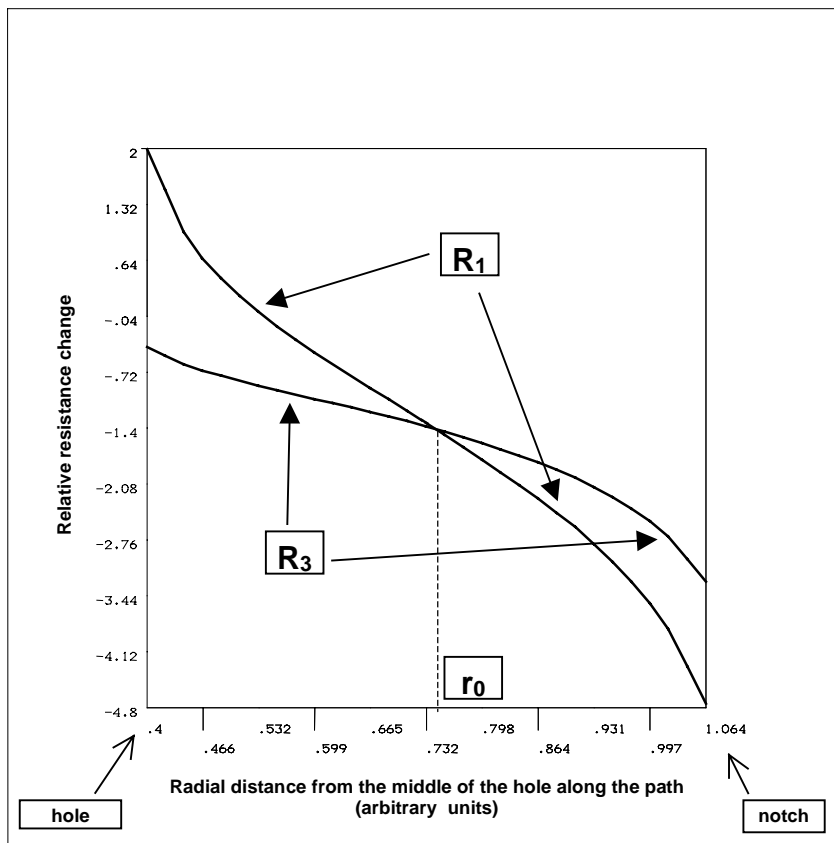


Fig. 11

Relative resistance change ($\Delta R_1/R$ and $\Delta R_3/R$) as a function of position of the middle points of the resistors 1 and 3 on the paths 1 and 3 in Fig.7, for a combined moment about the y-axis (M_y) and the shear force load in the x-direction, (F_x). Both loads are applied at the free end of the sensor (Fig. 10)

Due to symmetry reasons, the resistance changes ΔR_2 and ΔR_4 are in this case:

$$(15) \quad \Delta R_2 = -\Delta R_3 \text{ and } \Delta R_4 = -\Delta R_1$$

We noticed that independent of the separate values of shear forces and bending moments, the function values of the curves in Fig. 11 vary, but their overall shape, and in particular, the point of intersection of these two signals, r_0 , always remains the same!

3.3 Bending compensation

This led us to a straightforward conclusion: If all 4 resistors are positioned at the distance r_0 from the edge of the inner hole along the paths in Fig.7, the Wheatstone bridge is "blind" with respect to bending or shear force loading: The bridge signal builds the difference between the resistors 1 and 3 (and 2 and 4) which is exactly zero at the position r_0 . **For the resistors at r_0 the bridge is theoretically exactly compensated concerning bending and shear force loading!**

3.4 More than bending compensation

However, these numerical studies revealed more than this originally desired compensation: It turned out that the two signals always cross at r_0 . Guided by a simple physical reasoning, we attempted a Taylor expansion of the signal for the resistors 1 and 3 around the point r_0 . After several numerical studies it turned out that this Taylor expansion looks like

$$(16) \quad \frac{\Delta R_1(r)}{R} = A_S \cdot M_Y(z_C) + [B_S \cdot M_Y(z_C) + C_S \cdot F_X(z_C)] \cdot (r - r_0) + O(r - r_0)^3$$

$$(17) \quad \frac{\Delta R_3(r)}{R} = A_S \cdot M_Y(z_C) + [B_S \cdot M_Y(z_C) - C_S \cdot F_X(z_C)] \cdot (r - r_0) + O(r - r_0)^3$$

$M_Y(z_C)$ is the bending moment value about the stiff bending axis (y-axis, Fig. 10) and $F_X(z_C)$ is the shear force in the direction of the stiff bending axis (x-axis, Fig.7) in the cutting plane at the position z_C . This cutting plane is normal to the long axis of the sensor (through the middle of the central hole in Fig.7). A_S , B_S and C_S are constant factors, which depend on the exact sensor shape and dimensions, as well as on its material and the resistor properties

The signal dependencies in eqs. (16)-(17) lead to straightforward conclusions that by connecting the resistors differently, another quantities can be sensed:

3.5 Bending moment sensor

The resistors in Fig.8 can be connected according to the following scheme:

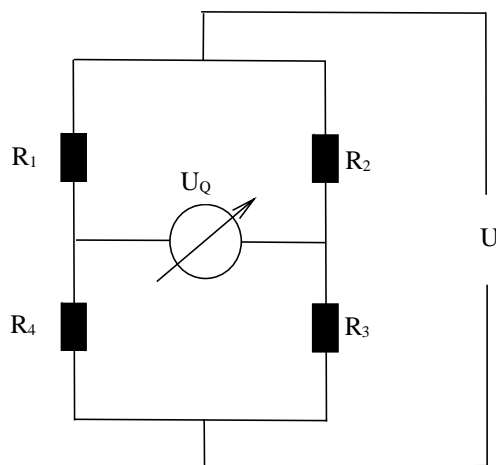


Fig. 12:
Resistor coupling scheme for a bending moment sensor.

The signal following from the scheme in Fig. 12 is

$$(18) \quad U_Q = U \cdot \frac{1}{4R} (\Delta R_1 + \Delta R_3 - \Delta R_2 - \Delta R_4)$$

At the position r_0 (Fig. 11) the relation $\Delta R_1 = \Delta R_3$ is valid. Under consideration of eq. (15) also the relation $\Delta R_2 = \Delta R_4$ applies. Thus, it follows from eqs. (16) and (17) that in a linear regime

$$(19) \quad U_Q = U \cdot A_S \cdot M_Y(z_C)$$

The signal from this scheme is at the same time insensitive to torsion, since from the symmetry arguments under torsion:

$$(20) \quad \Delta R_1 = \Delta R_2 \text{ and } \Delta R_3 = \Delta R_4$$

whereby the bridge signal $U_Q = 0$ results through the formula (18). **In this way we designed a perfectly compensated bending moment sensor with respect to the bending around the stiff axis!**

3.6 Shear force sensor

For the resistors connected according to the scheme in Fig. 9, but positioned at $r \neq r_0$ it follows from eqs. (14)-(17) that for mixed bending- and shear force loading, the sensor cell is blind for bending, but senses only the shear force in direction of the hard axis. Up to the linear terms:

$$(21) \quad U_Q = U \cdot C_S \cdot F_X(z_C) \cdot (r - r_0)$$

However, this scheme is, of course, sensitive to torsion.

In order to obtain the pure shear force signal, one can introduce additional 4 resistors, positioned at $r = r_0$, connected according to the scheme in Fig. 9. As explained before, this bridge measures a pure torsion and is blind for shear force and bending moments. One can subsequently build a difference signal between the two cells, thus retaining the pure shear force contribution, eq. (21).

3.7 General bending about the soft axis.

This is a case of a combined loading: A torque about the x-axis (M_X) and the shear force load in the y-direction, (F_Y). Both loads are applied at the free end of the sensor (Fig. 9).

Due to symmetry reasons, for an arbitrary bending around the x-axis and the shear force in the y-axis the following relation is valid:

$$(22) \quad \Delta R_1 = \Delta R_4 \text{ and } \Delta R_2 = \Delta R_3 \text{ for an arbitrary position } r.$$

Therefore, any of the resistor coupling schemes in this article is insensitive with respect to bending along the easy axis.

3.8 Conclusion

This FEA work led to the design, amplifying the torsion signal **by more than a factor of 5** with respect to the starting design concept. Moreover, based on originally purely numerical ANSYS results, it turned out, **a posteriori**, that a systematic, closed-form mathematical signal dependence on the resistor position exists (eqs. (17), (18)), for all the load cases of interest. These relations then straightforwardly revealed, that by slightly modifying the original sensor, two additional physical quantities can be sensed, all of them theoretically exactly compensated with respect to the undesired effects.

4 References

- [1] Jackson, J.D.: „Classical Electrodynamics“, John Wiley and Sons, Problem 5.11.
- [2] ibid., Chap. 5.

5 Acknowledgments

The calculations in Section 2 have been performed in cooperation with my colleague, Dr. Sven Kretzschmar. Besides Dr. Kretzschmar and myself, Mr. Bernd Rumpf is the third co-author of our patent application, related to these results.

Mr. Wolfgang Porth, Mr. Jürgen Irion and I are the co-authors of our two further patent applications, related to the results of Section 3.

I would like to thank the top technical R&D managers of VDO Fuel Systems: Mr. Bernd Rumpf, Mr. Helmut Kohlhaas and Dr. Wolfgang Sinz for their engaged support of this presentation.

I am also indebted to my very good colleagues, Mr. Hans Dieter Wilhelm, and Mr. Karl Eck, for daily creative discussions on FEA problems and other general physical and technical questions, concerning our products. These colleagues have strongly contributed to creation of an exceptionally innovative atmosphere, nourishing the development of the analysis activity at VDO Fuel Systems.

Many thanks are also due to Mr. Steve Pilz of ANSYS Inc, who, knowing the content of our work, came out with an idea about an article, highlighting the emphasis on physical reasoning using ANSYS in different fields, and who proposed the title of this paper!